RSC Advances

ROYAL SOCIETY OF CHEMISTRY

PAPER

View Article Online
View Journal | View Issue

Check for updates

Cite this: *RSC Adv.*, 2020, **10**, 2581

Self-assembled $CeVO_4$/Au heterojunction nanocrystals for photothermal/photoacoustic bimodal imaging-guided phototherapy†

Junrong Wang,[a] Yubo Hu,[b] Junyang Chen[b] and Cong Ye *[a]

Received 25th November 2019
Accepted 4th January 2020

DOI: 10.1039/c9ra09860g

rsc.li/rsc-advances

Phototherapy, including photothermal therapy (PTT) and photodynamic therapy (PDT), has attracted great attention because it can effectively inhibit the proliferation and propagation of cancer cells. Recently, heterojunction nanomaterials have shown tremendous application value in the field of biological medicine. In this work, the $CeVO_4$/Au heterojunction nanocrystals (NCs) are designed for photothermal/photoacoustic bimodal imaging-guided phototherapy. The as-synthesized hydrophobic oleic acid (OA)-stabilized $CeVO_4$ nanosheets were modified with HS-PEG-OH for translating into hydrophilic ones, which can significantly improve their stability and biocompatibility. Subsequently, the plasmonic Au nanoparticles were *in situ* successfully deposited on the surface of HS-PEG-coated $CeVO_4$ to form $CeVO_4$/Au heterojunction NCs for improving the visible and near-infrared light absorption, which results in enhanced photothermal conversion performance and reactive oxygen species (ROS) generation capacity. Thus, the $CeVO_4$/Au can cause more severe damage to cancer cells than pure $CeVO_4$ under NIR laser irradiation. Also, $CeVO_4$/Au can provide distinct tumor contrast by photothermal/photoacoustic bimodal bioimaging. Our results demonstrate that $CeVO_4$/Au NCs could be used as an effective theranostic anticancer agent for near-infrared (NIR) light-mediated PTT and PDT.

Introduction

Cancer has a very serious impact on human health, which causes high mortality worldwide.[1–5] Although surgery,[6] chemotherapy[7–9] and radiotherapy[10,11] are considered to be the main treatment approaches for cancer, they have many disadvantages, such as surgical risks and complications, serious side effects and the metastasis of residual cancer cells. Phototherapy, including photothermal and photodynamic therapy, was identified as an emerging noninvasive treatment method and has become a powerful candidate to replace traditional therapeutic methods because it can effectively inhibit the proliferation and propagation of cancer cells.[12–14] Photothermal therapy (PTT) can effectively kill target cancer cells by utilizing NIR laser irradiation to produce heat energy from light energy.[15–17] In recent years, a series of photothermal agents, including gold nanoparticles (NPs),[18–20] carbon-based nanosheets,[21] metal chalcogenides,[22–25] and conjugated polymers[26,27] have been used in PTT. Photodynamic therapy (PDT) can transfer the absorbed light to produce toxic reactive oxygen species (ROS) under NIR laser irradiation by exciting the photosensitizer molecules, in particular oxidative species ($\cdot O_2^-$) can cause significant cancer cell apoptosis and necrosis.[13,28,29] Recently, the semiconductor NPs (such as TiO_2,[30] ZnO,[31] $Fe_3O_4@SiO_2$–CdTe[32]), metal phthalocyanines,[33] and chlorin derivatives[34] have been used as photosensitizers for PDT by exciting the electron–hole pairs separation. In addition, the imaging technology such as photothermal (PT) imaging and photoacoustic (PA) imaging has been introduced for accurate diagnosis and treatment of cancer. The PT imaging can directly show the therapeutic effect of PTT through monitoring macroscopic temperature change. And the (PA) imaging provides a promising biomedical imaging modality, which provides higher spatial resolution and relatively deeper tissue penetration through the detection of ultrasonic signal waves.[35–37]

Inorganic semiconductor nanomaterials have been widely used as photothermal agents,[38] photosensitizes[39] and multimode imaging agents[40–42] due to their unique optical performance. Cerium vanadate ($CeVO_4$), a kind of wide band gap inorganic semiconductor nanomaterials,[43] has relatively small optical cross-sections in the Vis/NIR regions.[44] Thus, it was rarely applied as NIR-responsive anticancer agents.[45] The local surface plasmon resonance (LSPR)[46] offers a new strategy to enhance the optical absorption of semiconductor nanomaterials through loading plasmonic metal nanoparticles (NPs)

---

[a] Department of Obstetrics and Gynecology, China-Japan Union Hospital of Jilin University, Changchun, Jilin 130033, China. E-mail: zhanggs576@163.com

[b] Department of Anesthesiology, China-Japan Union Hospital of Jilin University, Changchun, Jilin 130033, China

† Electronic supplementary information (ESI) available: Experimental section, zeta potential, hydrodynamic size, photothermal activity, DPBF depletion, MB depletion, linear relationship between PA signal and sample concentration, blood panel and serum biochemical index parameters. See DOI: 10.1039/c9ra09860g

on the surface of semiconductor NCs.[47–51] Integrating plasmonic Au NPs with various semiconductors nanomaterials to form heterojunction nanostructures, such as Au@SiO_2@Cu_2O,[52] Bi_2S_3@Au,[53] Au@CuS,[54] CuS@Cu_2S@Au,[55] Au/TiO_2,[56] Au@PB@Cu_2O@ BPQDs/PAH,[57] Au@$NdVO_4$,[49] Au/Fe_3O_4,[58] could significantly expand the light absorption range to improve the photo-conversion performance.

Herein, we have successfully obtained $CeVO_4$/Au heterojunction NCs in this study (Scheme 1). Firstly, the oleic acid (OA)-stabilized $CeVO_4$ nanosheets were prepared through hydrothermal method.[59] Next, the (OA)-stabilized $CeVO_4$ was modified by HS-PEG-OH through thiolene click reaction. These modified materials can improved biocompatibility and stability.[32,60–64] Finally, Au NPs were *in situ* successfully deposited on the surface of HS-PEG-coated $CeVO_4$ to form $CeVO_4$/Au heterojunction NCs. Once $CeVO_4$/Au was transferred into water from THF, they presented self-assembled morphology due to hydrophobic–hydrophobic interactions because the OA-coated $CeVO_4$ didn't completely modified by HS-PEG-OH. Due to the LSPR effect of Au, the $CeVO_4$/Au NCs represents enhanced separation efficiency of electron and hole pairs and increased optical absorption in Vis/NIR region, resulting in improved ROS generation capability and photothermal conversion performance. Therefore, the $CeVO_4$/Au could cause severe damage to cancer cells than $CeVO_4$ under NIR laser irradiation. Also, the $CeVO_4$/Au can provide distinct tumor contrast by photothermal/photoacoustic bimodal bioimaging. Our results demonstrate that $CeVO_4$/Au NCs could be used as an effective theranostic anticancer agent for near-infrared (NIR) light-mediated PTT and PDT.

Experimental section

Synthesis of oleic acid-capped $CeVO_4$ nanosheets

NaOH (0.6 g) and NH_4VO_3 (0.0585 g) were added into 5 mL of deionized water under magnetic stir. A mixed solution of oleic acid (9 mL) and ethanol (10 mL) was added into the above solution. Then, 1 mL of $Ce(NO_3)_3 \cdot 6H_2O$ aqueous solution (1 M) was added dropwise. After stirring for 10 min, the mixed solution was sealed in a 40 mL Teflon-lined autoclave (140 °C, 8 h), then slowly cooled to room temperature, the samples were collected and dissolved in cyclohexane. Finally, $CeVO_4$ nanosheets were isolated by centrifugation at 3000 rpm (5 min), and washed with cyclohexane and ethanol. Afterward, the $CeVO_4$ nanosheets were distributed in 5 mL cyclohexane.

Synthesis of HS-PEG-functionalized $CeVO_4$ nanosheets

The 2 mL of above $CeVO_4$ nanosheets were precipitated by adding enough ethanol and isolated by centrifugation at 3000 rpm for 5 min. Then the samples were dissolved into 2 mL of THF solution. Then 0.2 g of HS-PEG-OH and 100 μL of photoinitiator DMPA (10 mg mL^{-1}) dissolved in THF were added. The mixture was irradiated with UV-light (1000 W, 365 nm wavelength) for 60 min in an ice bath under stirring. After completion of UV irradiation, the HS-PEG-functionalized $CeVO_4$ nanosheets were isolated by centrifugation at 12 000 rpm (15 min), and washed with water.

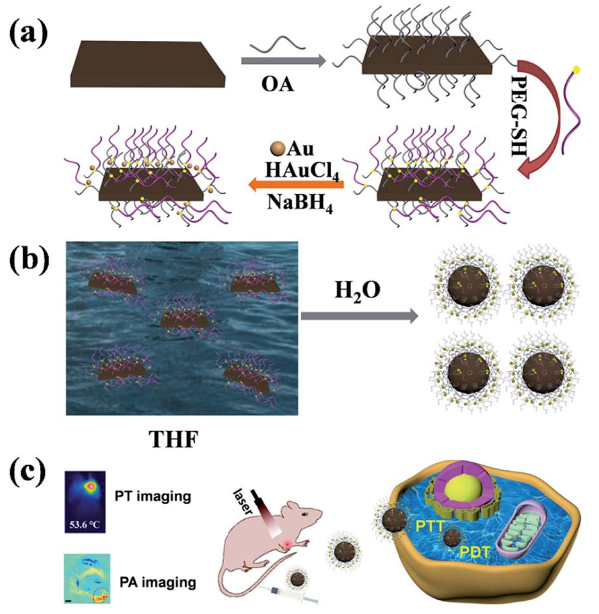

Scheme 1 Schematic illustration of the synthesis process (a), self-assembly process (b) and biological application (c) of $CeVO_4$/Au.

Synthesis of $CeVO_4$/Au heterojunction NCs

The above HS-PEG functionalized $CeVO_4$ nanosheet was distributed in ethanol (1.2 mL). After stirring for 30 min, 100 μL of $HAuCl_4 \cdot 3H_2O$ aqueous solution (0.029 M) was added. After stirring for 10 min, 50 μL of $NaBH_4$ (0.06 M) was added and stirred for 30 min. The $CeVO_4$/Au NCs were centrifuged at 12 000 rpm (10 min), and washed with ethanol. Afterward, the products were distributed in deionized water.

Toxicology evaluation

The $CeVO_4$/Au (20 mg kg^{-1}, 100 μL) was tail vein injected into healthy Blab/c mice and the mice injected with normal saline as a control group. For the blood of the experimental group and control group was collected (1 day, 7 days and 14 days post-injection). And then the blood panel and serum biochemical analysis were carried on.

Bio-distribution of $CeVO_4$/Au in mice

The $CeVO_4$/Au (20 mg kg^{-1}, 100 μL) was tail vein injected into U14 tumor-bearing Balb/c mice. Then the mice ($N = 4$) were euthanized at different time points (1 hour, 4 hours, 8 hours, 12 hours, 1 day, 3 days and 7 days). The major organs (heart, liver, spleen, lung, and kidney) and tumor were collected and weighed. Afterward, these organs were dealt with concentrated nitric acid and H_2O_2 [$V(HNO_3) : V(H_2O_2) = 1 : 2$] on heating (70 °C) until they became clear. The concentrations of Ce and Au were detected by inductively coupled plasma mass spectrometry (ICP-MS), and were calculated in each organ and tumor.

Live-dead cell staining experiments

HeLa cells were seeded at a density of 0.2×10^5 cells per well in 24-well culture plates and incubated at 37 °C in 5% CO_2 for 24 h. Afterward, HeLa cells were incubated with 400 μL of $CeVO_4$ or $CeVO_4$/Au (200 μg mL^{-1}) at 37 °C for 4 hours. Then, the culture media were replaced with fresh medium, and exposed to NIR laser irradiation (1.0 W cm^{-2}) for 5 min. After that, the live cells were stained with Calcein-AM (green fluorescence) and the dead cells were stained with pyridine iodide (PI) (red fluorescence).

Histological analysis

For hematoxylin and eosin (H&E) staining, major organs (heart, liver, spleen, lung, and kidney) and tumor were harvested, fixed in 10% neutral buffered formalin, processed routinely into paraffin, sectioned into thin slices and stained with H&E for histological analysis at day 14.

Photothermal (PT) imaging

For *in vitro* PT imaging, the $CeVO_4$ solution and $CeVO_4$/Au solution (200 μg mL^{-1}, 100 μL) were exposed to a cuvette and were placed on NIR laser irradiation (1.0 W cm^{-2}) for 5 min. The real-time temperature was detected and recorded by an infrared camera. For *in vivo* PT imaging, U14 cells were subcutaneously inoculated into the left armpit of Blab/c mice. While the tumor volume changes reached about 100 mm^3, normal saline (100 μL), $CeVO_4$ and $CeVO_4$/Au (20 mg kg^{-1}) were tail vein injected, respectively. After 8 h post-injection, the tumor was exposed to NIR laser irradiation (0.5 W cm^{-2}), and PT images were captured by an infrared camera.

Photoacoustic (PA) imaging

To measure the photoacoustic (PA) signal sensitivity of $CeVO_4$ and $CeVO_4$/Au, a phantom filled with the different concentrations of NCs (10, 20, 40, 80 and 160 μg mL^{-1}) was measured using a real-time multispectral optoacoustic tomographic (MSOT) imaging system (inVision 128, iThera Medical GmbH, Neuherberg, Germany). Subsequently, the phantom was placed into a water tank and imaged at the 680–980 nm laser. Finally, the PA signals were measured in regions of interest (ROIs) for each sample and the correlation between the PA signal and concentration response curve was calculated.

To perform *in vivo* PA imaging, $CeVO_4$ and $CeVO_4$/Au NCs (20 mg kg^{-1}, 100 μL) were tail vein injected into the tumor-bearing mice. After 8 h, the mice were placed in a container surrounded by a polyethylene film. In all data acquisitions, the light fibers and ultrasonic sensor arrays were in a fixed position. The mice were scanned before and after tail vein injection. ROIs were chosen and the PA signal was analyzed using ViewMOST™ software.

Animal xenograft model

Female Balb/c mice (six weeks old) were purchased from the Center for Experimental Animals, Jilin University. All animal studies were conducted in accordance with the guidelines of the National Regulation of China for Care and Use of Laboratory Animals. The U14 tumor models were successfully established by subcutaneous injection of 4×10^6 cells suspended in 100 μL PBS into the left armpit of each mouse. The mice were treated when the tumor volumes approached 100 mm^3.

Results and discussion

Preparation and characterization of the $CeVO_4$ and $CeVO_4$/Au

The preparation process of $CeVO_4$/Au was showed in Scheme 1. Firstly, the oleic acid (OA)-stabilized $CeVO_4$ nanosheets were prepared through the hydrothermal method,[59] which exhibits square-like sheet morphology as shown in the transmission electron microscopy (TEM) image (Fig. 1A). And the characteristic diffraction peaks of $CeVO_4$ in powder X-ray diffraction (XRD) patterns match well with those of the tetragonal phase ($CeVO_4$, JCPDS 82-1969) (Fig. 1B). Afterward, the (OA)-stabilized $CeVO_4$ surface was modified by the HS-PEG-OH[60] for transforming hydrophobic $CeVO_4$ into hydrophilic and enhancing biocompatibility. On the basis of the FT-IR spectroscopy (Fig. 1C), we concluded that the =C–H stretching vibration appears at 3006 cm^{-1} decreased and the stretching vibration owing to $-CH_2-O-$ at 1106 cm^{-1} is gradually enhanced, which demonstrate that the OA-stabilized $CeVO_4$ was successfully modified by HS-PEG-OH. Finally, Au nanoparticles were *in situ* deposited on the surface of HS-PEG-coated $CeVO_4$ *via* the reduction of $HAuCl_4$ by $NaBH_4$. Fig. 1D shows the TEM image of as-prepared $CeVO_4$/Au heterojunction nanocrystals, which presents self-assembled morphology due to hydrophobic–hydrophobic interactions because the OA-coated $CeVO_4$ didn't completely modified by HS-PEG-OH. According to the high-resolution transmission electron microscopy (HR-TEM) image (Fig. 1E), the lattice fringes of $CeVO_4$/Au nanohybrids display interplanar spacings of 0.2355 nm and 0.2949 nm, which match well with those of the (111) and the (211) planes of Au and $CeVO_4$, respectively. As can be seen from the elemental mapping (Fig. 1F), the elements of Ce, V, O, C, S and Au are

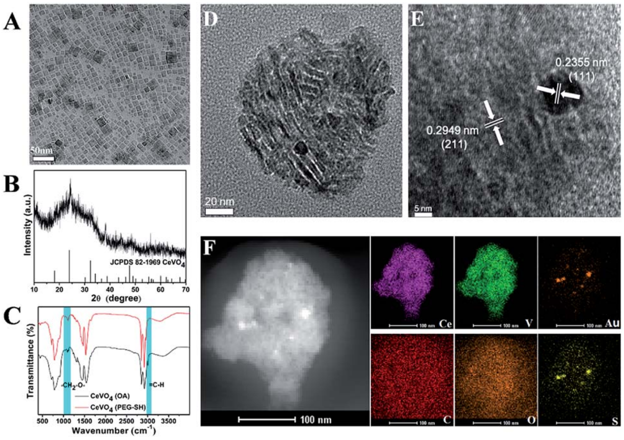

Fig. 1 (A) TEM images of the OA-capped $CeVO_4$ dispersed in hexane; (B) XRD patterns of OA-capped $CeVO_4$; (C) FTIR spectra of OA-capped $CeVO_4$ and CeVO4 modified by HS-PEG-OH; (D) TEM image of $CeVO_4$/Au; (E) HR-TEM image and (F) EDS elemental mapping of $CeVO_4$/Au.

presented in the $CeVO_4$/Au nanohybrids. And the changed zeta potential from 20.3 to −6.3 mV further verified the formation of $CeVO_4$/Au (Fig. S1†). Moreover, the average hydrodynamic particle sizes of $CeVO_4$/Au is about 127.5 nm, which could maintain constant within seven days in various physiological solutions (Fig. S2†).

Photothermal properties contrast among $CeVO_4$ and $CeVO_4$/Au

The $CeVO_4$/Au displays exceptional optical properties due to LSPR of Au NPs as compared to pure $CeVO_4$. According to the UV-Vis-NIR spectroscopy (Fig. 2A), a slight blue-shift of the Ce^{3+} characteristic absorption from 285 to 275 nm was observed due to the formation of $CeVO_4$/Au nanohybrids. More importantly, the obviously enhanced absorption of $CeVO_4$/Au could be found in the Vis/NIR region, which stimulated our study of the photothermal properties of $CeVO_4$/Au. The temperature elevation of $CeVO_4$, $CeVO_4$/Au, and water under NIR (1.0 W cm^{-2}) laser irradiation was showed in Fig. 2B. The temperature of $CeVO_4$/Au aqueous solution increased to 54.7 °C, while that of $CeVO_4$ solution and water only increase to 40 °C and 28.9 °C, respectively. In addition, both $CeVO_4$/Au and $CeVO_4$ showed concentration and power density-dependent temperature evolution activity (Fig. S3A–D†). However, the $CeVO_4$/Au solution displayed a more excellent photothermal conversion performance than pure $CeVO_4$ solution. According to the obtained test result (Fig. 2C and S4†), the time constant (τ_s) for the cooling process of $CeVO_4$/Au and $CeVO_4$ are determined to be 488.63 s and 581.51 s, respectively. Meanwhile, the photothermal conversion efficiency (η) of $CeVO_4$/Au and $CeVO_4$ were calculated to be 17.32% and 11.65%, respectively. Moreover, the photothermal conversion performance of $CeVO_4$/Au is almost no change after three cycles of heating and cooling (heating 6 min and cooling 12 min for one cycle, Fig. 2D). Collectively, these results validate that $CeVO_4$/Au heterojunction NCs are more excellent photothermal conversion agent than pure $CeVO_4$ due to the LSPR of Au NPs.

The ROS detection

The production capability of reactive oxygen species (ROS) over $CeVO_4$ and $CeVO_4$/Au heterojunction NCs upon NIR laser irradiation was further studied. As a result of LSPR excitation, Au NPs could generate hot electrons through absorbing resonant photons and transmit them to the adjacent $CeVO_4$, which surmounts the wide band gap of $CeVO_4$ and leads to effective separation of electrons–holes pairs in $CeVO_4$/Au heterojunction NCs. In the first place, Au NPs could produce hot electrons upon resonant excitation. These hot electrons could focus on the conduction band (CB) of the $CeVO_4$ by hot-electrons injection process,[65,66] and they could be seized by molecular oxygen (O_2) to produce $\cdot O_2^-$. The 1,3-diphenylisobenzofuran (DPBF) probe was used to monitor the performance of $CeVO_4$ and $CeVO_4$/Au to generate $\cdot O_2^-$ under photo-excitation. On the basis of Fig. 3A and S5,† we concluded that the absorption intensity of DPBF decreased distinctly with the increasing of NIR laser irradiation time in the $CeVO_4$/Au group, while that of the $CeVO_4$ group was almost unchanged. In order to eliminate the interference of oxygen, we detected the fluorescence intensity of singlet oxygen sensor green (SOSG, highly specific fluorescent indicator to $^1O_2$) in the presence of $CeVO_4$ and $CeVO_4$/Au with NIR laser (1.0 W cm^{-2}) irradiation. As displayed in Fig. S6,† we concluded that the fluorescence intensity of SOSG were almost unchanged with the increasing of NIR laser irradiation time in the $CeVO_4$/Au group and the $CeVO_4$ group. From the results we have obtained

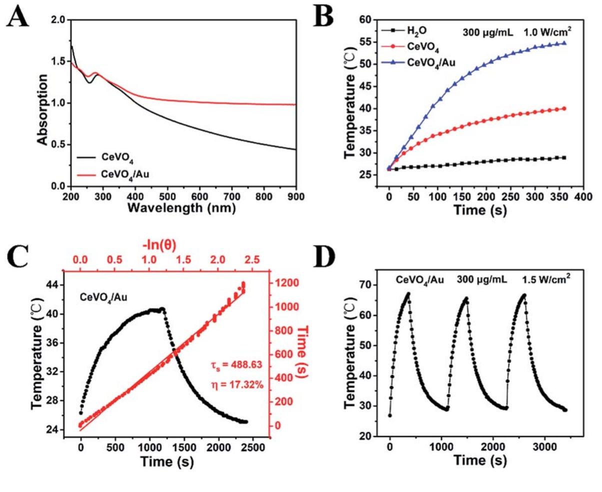

Fig. 2 (A) Vis/NIR absorption spectra of $CeVO_4$ and $CeVO_4$/Au. (B) Photothermal activity of $CeVO_4$ and $CeVO_4$/Au (300 μg mL^{-1}) under 1.0 W cm^{-2} of NIR laser irradiation for 5 min. (C) The temperature change of $CeVO_4$/Au aqueous solution (300 μg mL^{-1}, 1 mL) response to 1.3 W cm^{-2} of NIR laser on and off and Linear time data *versus* −ln θ obtained from the cooling period of $CeVO_4$/Au aqueous solution. (D) The PT conversion cycling test of $CeVO_4$/Au aqueous solution under 1.0 W cm^{-2} of NIR laser irradiation.

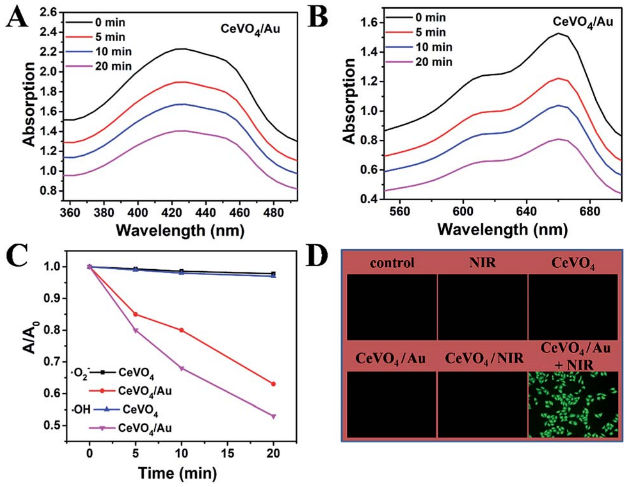

Fig. 3 (A) Depletion of DPBF due to $\cdot O_2^-$ generation: 65 μg mL^{-1} of $CeVO_4$/Au with NIR laser (1.0 W cm^{-2}) irradiation. (B) Depletion of MB due to ·OH generation: 65 μg mL^{-1} of $NdVO_4$/Au with NIR laser (1.0 W cm^{-2}) irradiation. (C) The comparison of ·OH and $\cdot O_2^-$ generating ability over $CeVO_4$ and $CeVO_4$/Au NCs plus NIR laser irradiation. (D) Fluorescence microscope images of ROS generation in HeLa cells that received different treatments.

no singlet oxygen ($^1O_2$) was generated. In the second place, the residual holes (h_{VB}^+) in the valence band of $CeVO_4$ could oxidize H_2O to produce hydroxyl radicals ($\cdot OH$), which was monitored by the degradation of methylene blue (MB). Comparing with the $CeVO_4$ group, the absorption intensity of MB decreased rapidly in the $CeVO_4$/Au group under NIR laser irradiated for 20 min (Fig. 3B and S7†). From the results we have obtained, the separation efficiency of electron/hole pairs of $CeVO_4$/Au was remarkably improved in comparison with that of $CeVO_4$ due to the LSPR of Au NPs, which leads to affluent ROS generation more effectively (Fig. 3C). In order to evaluate NIR-induced ROS generation in the cellular level, the ROS production was detected by non-fluorescent 2′,7′-dichlorodihydrofluoresceindiacetate (DCFH-DA), which can be oxidized by ROS translated into 2′,7′-dichlorofluorescein (DCF) with green fluorescence. As could be seen from Fig. 3D, no visible fluorescence was monitored in the control, NIR, $CeVO_4$, $CeVO_4$/Au, or $CeVO_4$ plus NIR groups. Nevertheless, the fluorescence of DCF (bright green) was showed in the group of $CeVO_4$/Au plus NIR groups, which further confirmed that the boosted ROS production ability of $CeVO_4$/Au owing to the LSPR of Au NPs.

Cellular uptake imaging, cytocompatibility, and cytotoxicity assay

On the basis of the boosted ROS production ability and photothermal performance of $CeVO_4$/Au, the synergistic photothermal and photodynamic anticancer effect *in vitro* was investigated. Before the *in vitro* anticancer application, the cellular uptake behavior of the $CeVO_4$/Au heterojunction NCs was verified. As displayed in Fig. 4A, the overlapping fluorescence of DAPI-labeled cell nuclei (blue) and rhodamine B (RhB)-labeled $CeVO_4$/Au (red) was observed, which suggested that the efficient uptake of $CeVO_4$/Au NCs *via* endocytosis. To further prove the cell uptake of $CeVO_4$/Au NCs was *via* endocytosis. We explore the intensity of red fluorescence from rhodamine B by different treatment times (HeLa cells treated with $CeVO_4$/Au NCs-RhB at different times, 0 h, 2 h, 4 h and 6 h), which was detected by flow cytometry. As displayed in Fig. S8,† with the increase in time, the red fluorescence intensity of rhodamine B raised, which indicated the increased cell endocytosis and the efficient uptake of $CeVO_4$/Au NCs by cell. The biocompatibility of $CeVO_4$ and $CeVO_4$/Au was monitored on HeLa and L929 cells *via* standard methyl thiazolyl tetrazolium (MTT) assay. As exhibited in Fig. 4B, both L929 and HeLa cell viability were unaffected even if the concentrations of $CeVO_4$/Au NCs up to 200 μg mL^{-1}, which identified that the $CeVO_4$ and $CeVO_4$/Au have well biocompatibility. Then the NIR-triggered photo-toxicity of $CeVO_4$ and $CeVO_4$/Au were assessed on HeLa cells. As could be seen from Fig. 4C and D, the cells mortality sharply rose to around 85% when HeLa cells were dealt with a low concentration (200 μg mL^{-1}) of $CeVO_4$/Au plus NIR (1.0 W cm^{-2}) irradiation. However, only about 23% of HeLa cells were killed in the $CeVO_4$ group even if the laser power density reached up to 1.5 W cm^{-2}. The outstanding killing capability of $CeVO_4$/Au to cancer cells were further confirmed *via* live-dead cell staining experiments (Fig. 4E). The above results demonstrated that the improved synergistic photothermal and photodynamic anticancer effect of $CeVO_4$/Au in comparison with single $CeVO_4$ *in vitro*, which was caused by boosted ROS production ability and photothermal performance of $CeVO_4$/Au.

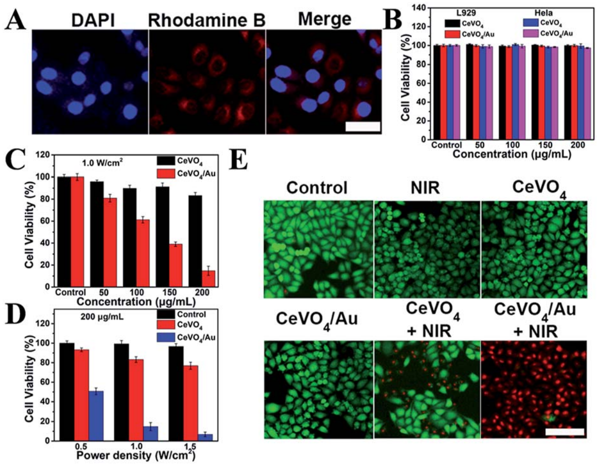

Fig. 4 (A) Cellular uptake of the $CeVO_4$/Au as detected in HeLa cells treated with $CeVO_4$/Au-RhB and DAPI. (B) L929 cell and HeLa cell viability when incubated with $CeVO_4$ and $CeVO_4$/Au for 24 h at different concentrations. (C) HeLa cell viability when incubated with different concentrations of $CeVO_4$ and $CeVO_4$/Au for 24 h under NIR laser irradiation at 1.0 W cm^{-2} for 5 min. (D) HeLa cell viability when incubated with $CeVO_4$ and $CeVO_4$/Au (200 μg mL^{-1}) for 24 h under NIR laser irradiation with different power densities for 5 min. (E) Live/dead cytotoxicity analysis of HeLa cells after different treatment. (Scale bar 50 μm).

PT/PA dual-modal imaging

Owing to the intrinsic absorption of $CeVO_4$ and $CeVO_4$/Au in the NIR region, their potentials as effective photothermal (PT) imaging and photoacoustic (PA) imaging[37] agents *in vitro* and *in vivo* were investigated. Firstly, the PT imaging capability *in vitro* was studied by irradiating deionized water, $CeVO_4$, and $CeVO_4$/Au solution with NIR laser irradiation (1.0 W cm^{-2}) for 5 min. Simultaneously, the real-time temperature changes were recorded prep 1 min by an infrared thermal camera. As displayed in Fig. 5A, the temperature of $CeVO_4$/Au and $CeVO_4$ could raise by about 21.6 °C and 10.7 °C, respectively. However, the temperature of the deionized water could only be enhanced by 2.3 °C. Whereafter, for *in vivo* PT imaging, tumor-bearing mice were tail vein injected with PBS, $CeVO_4$, and $CeVO_4$/Au (20 mg kg^{-1}) solution and were exposed to NIR laser irradiation (0.5 W cm^{-2}). All animal procedures were performed in accordance with the Guidelines for the Care and Use of Laboratory Animals of Jilin University (Changchun, China) and were approved by the Animal Ethics Committee of the National Regulation of China for the Care and Use of Laboratory Animals. And the real-time thermal images were detected by an infrared thermal camera. As could be seen from Fig. 5B, the tumor temperature in the mice injected with the $CeVO_4$/Au increased by about 16.7 °C, which is obviously higher than that of $CeVO_4$-injected mice (8.7 °C). While the tumor temperature of control group mice

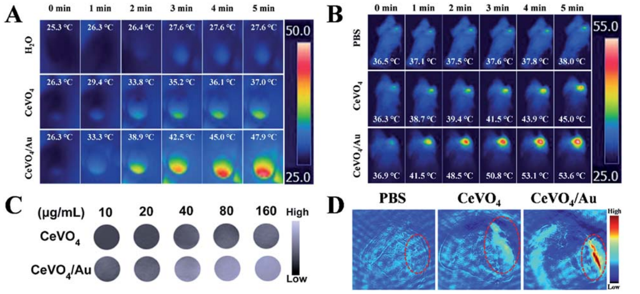

Fig. 5 (A) The thermal images of H_2O, $CeVO_4$ and $CeVO_4$/Au (200 μg mL^{-1}, 100 μL) exposed to NIR laser irradiation (1.0 W cm^{-2}) for different times (0, 1, 2, 3, 4 and 5 min). (B) The thermal images of U14-tumor-bearing mice with tail veins injection of normal saline, $CeVO_4$ and $CeVO_4$/Au (20 mg kg^{-1}, 100 μL) for 12 h exposed to NIR laser light irradiation (0.5 W cm^{-2}) for different times (0, 1, 2, 3, 4 and 5 min). (C) PA imaging phantoms, consisting of various concentrations of $CeVO_4$ and $CeVO_4$/Au embedded in agar gel cylinders. (D) PA images of tumor site after tail veins injection with normal saline, $CeVO_4$ and $CeVO_4$/Au (20 mg kg^{-1}, 100 μL) for 8 h. (The red circle is tumor sites.)

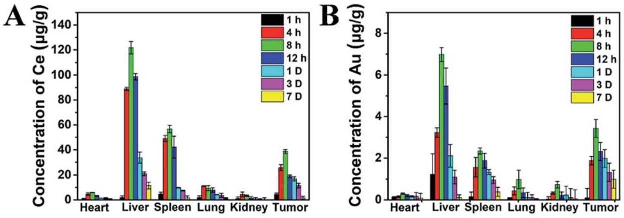

Fig. 6 Bio-distribution of Ce (A) and Au (B) in major organs and tumors of mice after injection of $CeVO_4$/Au (20 mg kg^{-1}, 100 μL) at different time points.

injected with PBS didn't show an evident increase. From the results, we concluded that the $CeVO_4$/Au has more excellent photothermal imaging ability than single $CeVO_4$. Then, the potential of $CeVO_4$ and $CeVO_4$/Au as a PA imaging agent *in vitro* and *in vivo* was evaluated. As far as is concerned *in vitro* PA imaging, the different concentrations of $CeVO_4$ and $CeVO_4$/Au were embedded in agar gel cylinders to generate PA imaging. As exhibited in Fig. 5C, PA signal intensity of $CeVO_4$/Au exhibited remarkably increased with elevated concentration from 10 to 160 μg mL^{-1} in comparison with single $CeVO_4$. And the quantitative analysis illustrated a linear relationship between the PA signal intensity and samples ($CeVO_4$ and $CeVO_4$/Au) concentrations from 10 to 160 μg mL^{-1} (Fig. S9†). To investigate *in vivo* PA imaging effect, tumor-bearing mice tail vein injected with PBS, $CeVO_4$, and $CeVO_4$/Au (20 mg kg^{-1}) solution were detected, respectively. As displayed in Fig. 5D, the tumor site of the $CeVO_4$/Au-injected group exhibited clearly stronger PA signals than a single $CeVO_4$ injection group, while almost no PA signals in the tumor site of the PBS injection group could be detected. From the above results we have obtained, one can conclude that $CeVO_4$/Au NCs could be used as an appropriate anticancer agent for PT and PA bimodal imaging in early cancer diagnosis and treatment for further clinical application.

In vivo long-term toxicity evaluation and tumor inhibition effect

To further explore the cancer therapeutic effects of $CeVO_4$/Au NCs *in vivo*, we assess the long-term toxicity of the $CeVO_4$/Au NCs firstly. The results were obtained by detecting bio-distribution, blood panel, and serum biochemical index. These tests were monitored by injecting $CeVO_4$/Au NCs into mice *via* tail vein. The tumor and main organs (heart, liver, spleen, lung, kidney) were resected from the mice at different time periods (1 hour, 4 hours, 8 hours, 12 hours, 1 day, 3 days and 7 days) of post-injection, and the contents of the Ce and Au were detected *via* ICP-MS. As can be seen from Fig. 6, Ce and Au were dispersed in every main organs and tumor, while we could observe that the liver and spleen have high concentrations of Ce (Fig. 6A) and Au (Fig. 6B) accumulation after 8 h post-injection due to the cancellation of exotic substances by the reticuloendothelial system and macrophage at early stages. With the passage of time, the concentrations of Au and Ce in the main organs gradually declined, and the mass of the $CeVO_4$/Au NCs were overtly eliminated from the spleen and liver at 7 d post-injection. From the bio-distribution experiment results, we can conclude that the $CeVO_4$/Au NCs could be accumulated in the tumor site owing to the enhanced permeability and retention (EPR) effect, and the most effective treatment time is about 8 h post-injection. To achieve a better understanding of the long-term toxicity of the $CeVO_4$/Au NCs *in vivo*, the blood panel, and serum biochemical index were also investigated. As shown in Table S1,† we can demonstrate that all the indexes were in good consistent with the normal range and very approaching to the control group, suggesting that no hepatic or renal necrocytosis and inflammatory response could be found. Based on the above results, the $CeVO_4$/Au NCs had no apparent toxicity effects on healthy mice, which could be used as potential cancer therapeutic and diagnostic agents *in vivo.*

Based on the distinguished photothermal conversion property, ROS production capability, and no obvious poison effects of $CeVO_4$/Au NCs, we future investigated tumor inhibition effect of $CeVO_4$/Au NCs *in vivo*. The U14 tumor-bearing mice were randomly divided into six groups: (a) control group (normal saline injection), (b) NIR, (c) $CeVO_4$ injection, (d) $CeVO_4$/Au injection, (e) $CeVO_4$ injection + NIR and (f) $CeVO_4$/Au injection + NIR. The laser irradiation was implemented under NIR laser irradiation (0.5 W cm^{-2}) for 5 min. The tumor volume changes were recorded every 2 d after treatment (14 d) (Fig. 7B). We could found that the tumor in these groups of control group, NIR, $CeVO_4$, and $CeVO_4$/Au exhibited rapid growth trend during the 14 days treatment. Nevertheless, the tumor growth was suppressed slightly in the group of $CeVO_4$ + NIR laser irradiation. It is noteworthy that no tumor growth was observed in $CeVO_4$/Au + NIR laser irradiation during the 14 days treatment. The results could be further verified by the photos and tumors resection of each photographs of mice and tumors after different treatment (Fig. 7A). As shown in Fig. 7C, the tumor sections were stained with hematoxylin and eosin (H&E), which prove that tumor tissues were injured severely *via* $CeVO_4$/Au + NIR laser irradiation and correspondingly slight damage

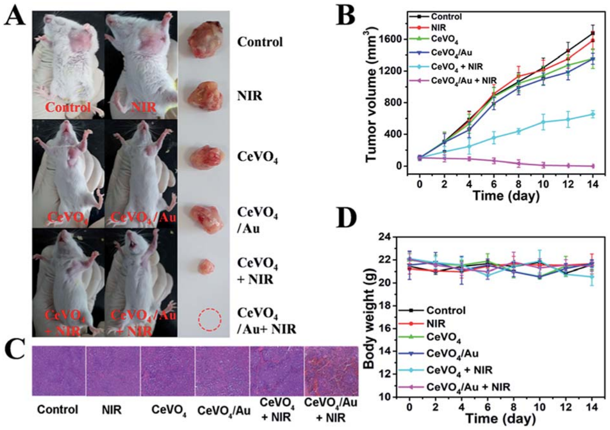

Fig. 7 (A) Photos of representative mice and excised tumor tissues from different groups at the end of treatment. (B) Relative tumor volumes changes, (C) images of H&E stained tumor sections and (D) body weight changes of different groups with different treatments processes ($n = 4$).

induced *via* $CeVO_4$ + NIR laser irradiation could also be observed. From the results we have obtained, the cancer therapy effect of $CeVO_4$/Au is very prominent than $CeVO_4$. Moreover, the body weights of these mice maintained growth steadily within 14 days in the different treatment groups (Fig. 7D). The main organs of mice after different treatments showed no obvious inflammatory lesion through histology analysis (Fig. 8). Taken together, $CeVO_4$/Au could be served as a PT/PA dual-modal imaging-guided anticancer agent, which possesses an enhanced antitumor effect than pure $CeVO_4$.

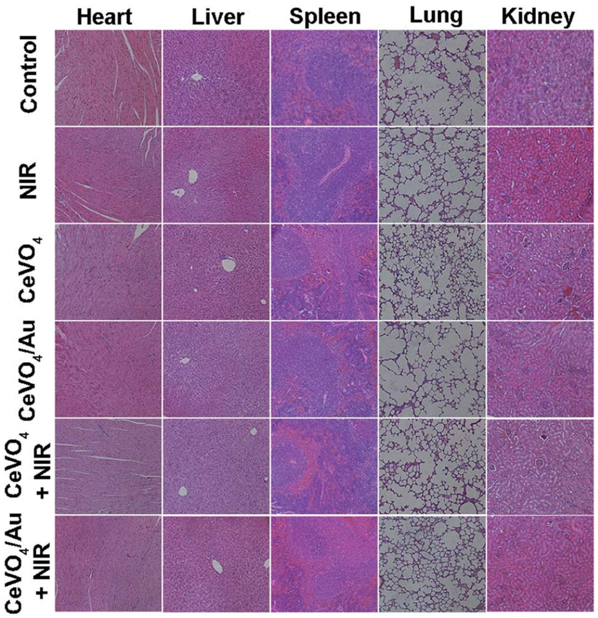

Fig. 8 The H&E stained images of major organs after the treatment with normal saline as control; NIR laser irradiation only; $CeVO_4$ only; $CeVO_4$/Au only; $CeVO_4$ + NIR laser irradiation; $CeVO_4$/Au + NIR laser irradiation (0.5 W cm^{-2}, 5 min).

Conclusions

In conclusion, the $CeVO_4$/Au heterojunction nanocrystals (NCs) were successfully fabricated in this study. The $CeVO_4$/Au NCs showed enhanced Vis/NIR light absorption and separation efficiency of electron and hole pairs because of the LSPR effect of Au NPs, which resulted in enhanced ROS generation capability and photothermal conversion ability than pure $CeVO_4$. The $CeVO_4$/Au could cause severe damage to cancer cells than $CeVO_4$ under NIR laser irradiation. Noteworthy, the $CeVO_4$/Au can provide distinct tumor contrast by photothermal/photoacoustic bimodal bioimaging. Also the $CeVO_4$/Au could act as NIR light-mediated photothermal therapy (PTT) and photodynamic therapy (PDT) anticancer agent, which presented enhanced tumor inhibition rate than pure $CeVO_4$. Taken together, our results demonstrate that $CeVO_4$/Au NCs could be used as an effective PT/PA bimodal imaging-guided theranostic anticancer agent for near-infrared (NIR) light-mediated PTT and PDT.

Conflicts of interest

There are no conflicts to declare.

Acknowledgements

This work was financially supported by the projects from Science and Technology department of Jilin province (no. 20190201003 JC; 3D518NU13430).

Notes and references

1 C. Zhang, W. H. Chen, L. H. Liu, W. X. Qiu, W. Y. Yu and X. Z. Zhang, *Adv. Funct. Mater.*, 2017, **27**, 1700626–1700639.
2 W. Fan, B. C. Yung and X. Chen, *Angew. Chem., Int. Ed.*, 2018, **57**, 8383–8394.
3 J. Xu, F. He, Z. Cheng, R. Lv, Y. Dai, A. Gulzar, B. Liu, H. Bi, D. Yang and S. Gai, *Chem. Mater.*, 2017, **29**, 7615–7628.
4 G. Yang, L. Xu, Y. Chao, J. Xu, X. Sun, Y. Wu, R. Peng and Z. Liu, *Nat. Commun.*, 2017, **8**, 902–914.
5 X. Zhu, J. Li, X. Qiu, Y. Liu, W. Feng and F. Li, *Nat. Commun.*, 2018, **9**, 2176–2186.
6 O. A. Martin, R. L. Anderson, K. Narayan and M. P. MacManus, *Nat. Rev. Clin. Oncol.*, 2017, **14**, 32–44.
7 L. Liao, J. Liu, E. C. Dreaden, S. W. Morton, K. E. Shopsowitz, P. T. Hammond and J. A. Johnson, *J. Am. Chem. Soc.*, 2014, **136**, 5896–5899.
8 Y. Wen, W. Zhang, N. Gong, Y.-F. Wang, H.-B. Guo, W. Guo, P. C. Wang and X.-J. Liang, *Nanoscale*, 2017, **9**, 14347–14356.
9 N. Shah, A. S. Mohammad, P. Saralkar, S. A. Sprowls, S. D. Vickers, D. John, R. M. Tallman, B. P. Lucke-Wold, K. E. Jarrell and M. Pinti, *Pharmacol. Res.*, 2018, **132**, 47–68.
10 Y.-S. Yang, R. P. Carney, F. Stellacci and D. J. Irvine, *ACS Nano*, 2014, **8**, 8992–9002.
11 K. Lu, C. He, N. Guo, C. Chan, K. Ni, G. Lan, H. Tang, C. Pelizzari, Y.-X. Fu and M. T. Spiotto, *Nat. Biomed. Eng.*, 2018, **2**, 600–610.

12 C. Liang, L. Xu, G. Song and Z. Liu, *Chem. Soc. Rev.*, 2016, **45**, 6250–6269.

13 W. Fan, P. Huang and X. Chen, *Chem. Soc. Rev.*, 2016, **45**, 6488–6519.

14 Z. Wan, H. Mao, M. Guo, Y. Li, A. Zhu, H. Yang, H. He, J. Shen, L. Zhou and Z. Jiang, *Theranostics*, 2014, **4**, 399–411.

15 D. Jaque, L. M. Maestro, B. Del Rosal, P. Haro-Gonzalez, A. Benayas, J. Plaza, E. M. Rodriguez and J. G. Sole, *nanoscale*, 2014, **6**, 9494–9530.

16 Y. Liu, P. Bhattarai, Z. Dai and X. Chen, *Chem. Soc. Rev.*, 2019, **48**, 2053–2108.

17 T. Ramasamy, H. B. Ruttala, P. Sundaramoorthy, B. K. Poudel, Y. S. Youn, S. K. Ku, H.-G. Choi, C. S. Yong and J. O. Kim, *NPG Asia Mater.*, 2018, **10**, 197–216.

18 X. Yang, M. Yang, B. Pang, M. Vara and Y. Xia, *Chem. Rev.*, 2015, **115**, 10410–10488.

19 J. Nam, N. Won, H. Jin, H. Chung and S. Kim, *J. Am. Chem. Soc.*, 2009, **131**, 13639–13645.

20 Y. Yang, M. Chen, Y. Wu, P. Wang, Y. Zhao, W. Zhu, Z. Song and X.-B. Zhang, *RSC Adv.*, 2019, **9**, 28541.

21 X. Zhu, W. Feng, J. Chang, Y.-W. Tan, J. Li, M. Chen, Y. Sun and F. Li, *Nat. Commun.*, 2016, **7**, 10437–10446.

22 M. Chang, M. Wang, M. Wang, M. Shu, B. Ding, C. Li, M. Pang, S. Cui, Z. Hou and J. Lin, *Adv. Mater.*, 2019, 1905271–1905280.

23 B. Ding, C. Yu, C. Li, X. Deng, J. Ding, Z. Cheng, B. Xing and J. Lin, *Nanoscale*, 2017, **9**, 16937–16949.

24 Y. Wang, D. Cai, H. Wu, Y. Fu, Y. Cao, Y. Zhang, D. Wu, Q. Tian and S. Yang, *Nanoscale*, 2018, **10**, 4452–4462.

25 B. Zhou, J. Zhao, Y. Qiao, Q. Wei, J. He, W. Li, D. Zhong, F. Ma, Y. Li and M. Zhou, *Appl. Mater. Today*, 2018, **13**, 285–297.

26 C. Hu, Z. Zhang, S. Liu, X. Liu and M. Pang, *ACS Appl. Mater. Interfaces*, 2019, **11**, 23072–23082.

27 Y. Shi, S. Liu, Y. Liu, C. Sun, M. Chang, X. Zhao, C. Hu and M. Pang, *ACS Appl. Mater. Interfaces*, 2019, **11**, 12321–12326.

28 C. Pais-Silva, D. de Melo-Diogo and I. Correia, *Eur. J. Pharm. Biopharm.*, 2017, **113**, 108–117.

29 X. Hu, H. Tian, W. Jiang, A. Song, Z. Li and Y. Luan, *Small*, 2018, **14**, 1802994–1803004.

30 D. Yang, G. Yang, Q. Sun, S. Gai, F. He, Y. Dai, C. Zhong and P. Yang, *Adv. Healthc. Mater.*, 2018, **7**, 1800042–1800052.

31 P. Sivakumar, M. Lee, Y.-S. Kim and M. S. Shim, *J. Mater. Chem. B*, 2018, **6**, 4852–4871.

32 Z. Wang, X. Jiang, W. Liu, G. Lu and X. Huang, *Sci. China: Chem.*, 2019, **62**, 889–896.

33 C. Yue, Y. Yang, C. Zhang, G. Alfranca, S. Cheng, L. Ma, Y. Liu, X. Zhi, J. Ni and W. Jiang, *Theranostics*, 2016, **6**, 2352–2366.

34 L. Zeng, Y. Pan, R. Zou, J. Zhang, Y. Tian, Z. Teng, S. Wang, W. Ren, X. Xiao and J. Zhang, *Biomaterials*, 2016, **103**, 116–127.

35 J. R. Cook, W. Frey and S. Emelianov, *ACS Nano*, 2013, **7**, 1272–1280.

36 F. Mao, L. Wen, C. Sun, S. Zhang, G. Wang, J. Zeng, Y. Wang, J. Ma, M. Gao and Z. Li, *ACS Nano*, 2016, **10**, 11145–11155.

37 Q. Miao and K. Pu, *Adv. Mater.*, 2018, **30**, 1801778–1801800.

38 Q. Tian, F. Jiang, R. Zou, Q. Liu, Z. Chen, M. Zhu, S. Yang, J. Wang, J. Wang and J. Hu, *ACS Nano*, 2011, **5**, 9761–9771.

39 W. Li, D. Li, S. Meng, W. Chen, X. Fu and Y. Shao, *Environ. Sci. Technol.*, 2011, **45**, 2987–2993.

40 Z. F. Huang, J. Song, L. Pan, X. Zhang, L. Wang and J. J. Zou, *Adv. Mater.*, 2015, **27**, 5309–5327.

41 H. Huang, K. Li, Q. Liu, Y. Zhao, H. Xu, W. Wu, K. Sun, J. Ni and J. Lin, *RSC Adv.*, 2019, **9**, 2718–2730.

42 C. Xia, D. Xie, L. Xiong, Q. Zhang, Y. Wang, Z. Wang, Y. Wang, B. Li and C. Zhang, *RSC Adv.*, 2018, **8**, 27382–27389.

43 A. Watanabe, *J. Solid State Chem.*, 2000, **153**, 174–179.

44 M. Conrad, F. Wang, M. Nevius, K. Jinkins, A. Celis, M. Narayanan Nair, A. Taleb-Ibrahimi, A. Tejeda, Y. Garreau and A. Vlad, *Nano Lett.*, 2016, **17**, 341–347.

45 G. Lu, X. Zou, F. Wang, H. Wang and W. Li, *Mater. Lett.*, 2017, **195**, 168–171.

46 X. Ding, C. H. Liow, M. Zhang, R. Huang, C. Li, H. Shen, M. Liu, Y. Zou, N. Gao and Z. Zhang, *J. Am. Chem. Soc.*, 2014, **136**, 15684–15693.

47 Y. Peng, Y. Liu, X. Lu, S. Wang, M. Chen, W. Huang, Z. Wu, G. Lu and L. Nie, *J. Mater. Chem. B*, 2018, **6**, 2813–2820.

48 M. Chang, M. Wang, Y. Chen, M. Shu, Y. Zhao, B. Ding, Z. Hou and J. Lin, *Nanoscale*, 2019, **11**, 10129–10136.

49 M. Chang, M. Wang, M. Shu, Y. Zhao, B. Ding, S. Huang, Z. Hou, G. Han and J. Lin, *Acta Biomater.*, 2019, **99**, 295–306.

50 W. Cao, X. Wang, L. Song, P. Wang, X. Hou, H. Zhang, X. Tian, X. Liu and Y. Zhang, *RSC Adv.*, 2019, **9**, 18874–18887.

51 M. H. Huang, S. Rej and C. Y. Chiu, *Small*, 2015, **11**, 2716–2726.

52 C. Liu, H. Dong, N. Wu, Y. Cao and X. Zhang, *ACS Appl. Mater. Interfaces*, 2018, **10**, 6991–7002.

53 Y. Cheng, Y. Chang, Y. Feng, H. Jian, Z. Tang and H. Zhang, *Angew. Chem., Int. Ed.*, 2018, **57**, 246–251.

54 Y. Chang, Y. Cheng, Y. Feng, H. Jian, L. Wang, X. Ma, X. Li and H. Zhang, *Nano Lett.*, 2018, **18**, 886–897.

55 X. Deng, K. Li, X. Cai, B. Liu, Y. Wei, K. Deng, Z. Xie, Z. Wu, P. a. Ma and Z. Hou, *Adv. Mater.*, 2017, **29**, 1701266–1701274.

56 A. Tanaka, S. Sakaguchi, K. Hashimoto and H. Kominami, *ACS Catal.*, 2012, **3**, 79–85.

57 T. Zheng, T. Zhou, X. Feng, J. Shen, M. Zhang and Y. Sun, *ACS Appl. Mater. Interfaces*, 2019, **11**, 31615–31626.

58 Q. Gao, A. Zhao, H. Guo, X. Chen, Z. Gan, W. Tao, M. Zhang, R. Wu and Z. Li, *Dalton Trans.*, 2014, **43**, 7998–8006.

59 J. Liu and Y. Li, *J. Mater. Chem.*, 2007, **17**, 1797–1803.

60 B. Liu, X. Deng, Z. Xie, Z. Cheng, P. Yang and J. Lin, *Adv. Mater.*, 2017, **29**, 1604878–1604886.

61 C. Feng and X. Huang, *Acc. Chem. Res.*, 2018, **51**, 2314–2323.

62 B. Xu, Y. Liu, X. Sun, J. Hu, P. Shi and X. Huang, *ACS Appl. Mater. Interfaces*, 2017, **9**, 16517–16523.

63 Y. Que, Y. Liu, W. Tan, C. Feng, P. Shi, Y. Li and H. Xiaoyu, *ACS Macro Lett.*, 2016, **5**, 168–173.

64 Y. Que, Z. Huang, C. Feng, Y. Yang and X. Huang, *ACS Macro Lett.*, 2016, **5**, 1339–1343.

65 R. Jiang, B. Li, C. Fang and J. Wang, *Adv. Mater.*, 2014, **26**, 5274–5309.

66 Q. Wu, M. Si, B. Zhang, K. Zhang, H. Li, L. Mi, Y. Jiang, Y. Rong, J. Chen and Y. Fang, *Nanotechnology*, 2018, **29**, 295702–295712.